

Effect of High Temperature Corrosion on the Service Life of P91 Piping in Biomass Co-firing

C.P. O'Hagan

Mechanical Engineering, College of Engineering & Informatics, NUI Galway, Ireland
Ryan Institute for Environmental, Marine and Energy Research, NUI Galway, Ireland
Mechanical Engineering, College of Engineering & Informatics, Engineering Building, NUI Galway, Ireland
c.ohagan1@nuigalway.ie

R.A. Barrett

Mechanical Engineering, College of Engineering & Informatics, NUI Galway, Ireland
Ryan Institute for Environmental, Marine and Energy Research, NUI Galway, Ireland
Mechanical Engineering, College of Engineering & Informatics, Engineering Building, NUI Galway, Ireland
Richard.Barrett@nuigalway.ie

S.B. Leen

Mechanical Engineering, College of Engineering & Informatics, NUI Galway, Ireland
Ryan Institute for Environmental, Marine and Energy Research, NUI Galway, Ireland
Mechanical Engineering, College of Engineering & Informatics, Engineering Building, NUI Galway, Ireland
Sean.Leen@nuigalway.ie

R.F.D. Monaghan

Mechanical Engineering, College of Engineering & Informatics, NUI Galway, Ireland
Ryan Institute for Environmental, Marine and Energy Research, NUI Galway, Ireland
Combustion Chemistry Centre, National University of Ireland, Galway, Ireland
Mechanical Engineering, College of Engineering & Informatics, Engineering Building, NUI Galway, Ireland
Rory.Monaghan@nuigalway.ie

¹Corresponding author. Email address: sean.leen@nuigalway.ie. Tel: +353(91)495955.

ABSTRACT

Co-firing biomass with fossil fuels is increasingly relevant to thermal power plant operators due to increasingly stringent regulations on greenhouse gas emissions. It has been found that the use of biomass results in an altered ash composition, which leads to increased corrosion of the superheater tube walls. A synthetic salt representative of the ash formed from co-firing a 70% peat and 30% biomass has been produced and applied to P91 samples at 540 °C for up to 28 days. This paper presents results for oxide layer thickness and loss of substrate from testing. Scanning electron microscopy (SEM) images and energy-dispersive x-ray spectroscopy (EDX) element maps are obtained and presented in order to gain an understanding of the complex corrosion mechanism which occurs. A finite element methodology is presented which combines corrosion effects with creep damage in pressurized tubes. The effect of corrosion tube wall loss and creep damage on tube stresses and creep rupture life is investigated.

1. INTRODUCTION

As a result of worldwide efforts to decarbonize its electricity generation capacity, the co-firing of biomass with fossil fuels is of increasing interest to power plant operators. This research focuses on peat-fired power plants and the response of superheater tube materials, specifically P91 steel, to the altered ash composition which is formed during biomass co-firing. The altered ash composition can lead to severe fireside corrosion of superheater and reheater tubing, resulting in a decreased life expectancy [1]–[3].

P91 is a 9Cr-1Mo martensitic steel, which has a complex hierarchical microstructure consisting of prior austenite grains, containing packets, blocks, laths (sub-grains), $M_{23}C_6$ (M=Cr, Mo, Fe) carbonitrides dispersed along the sub-grain boundaries and NbC/VC precipitates within the grains resulting in an improved creep strength [4]–[6]. This complex microstructure provides increased mechanical performance and in particular, results in a high creep strength and increased resistance to thermal fatigue.

Superheater tubes typically carry the highest pressure and highest temperature steam, while also being exposed to high temperature combustion flue gases. Due to this, superheater tubes are more susceptible to high temperature creep and corrosion failures than furnace walls and economizer tubes, which operate at lower temperatures [7]. Approximately 90% of failures due to high temperature creep or long-term overheating occurs in the superheater and reheater tubes [8]. Creep rupture failure of

the superheater and reheater tubes is a primary cause ($\approx 30\%$) of forced outages at coal and biomass fired boilers [9].

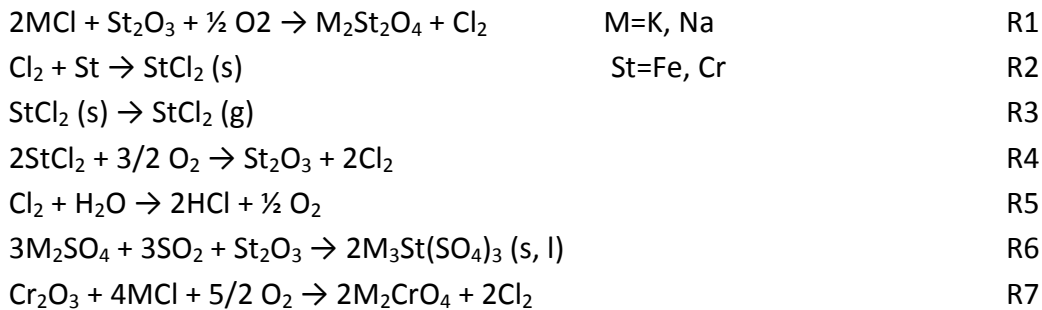
Finite element (FE) analysis of pipes subjected to creep damage has previously been carried out by Hyde et al. [10], [11], among many others. Separate FE models have also been developed to model corrosion of tube walls. Wenman et al. [12] model pitting corrosion and stress corrosion cracking via element removal in the FE code Abaqus, thus allowing for prediction of stress redistribution and subsequent crack growth.

Sawada et al. [13] have investigated the effect of oxidation on the creep strength of T23 steel in air and in helium and found that at $625\text{ }^{\circ}\text{C}$ there was no noticeable effect of oxidation; however at $650\text{ }^{\circ}\text{C}$ oxide scales were found to contribute to creep strength degradation. As these tests were carried out in air, without deposits, it is expected that they would have lower corrosion rates than those carried out exposed to harmful deposits.

Additionally, work by Fournier et al. [14]–[16] has attempted to combine creep, fatigue and oxidation effects in order to obtain lifetime predictions. Fournier et al, have found that the environment plays a major role both in crack initiation and propagation [16]. In general the corrosion resistance of tubing alloys increases with an increase in chromium content [17], [18]. Additionally it has been noted that the corrosion caused by coal ash is quite different than that caused by other fuels and is, at least partially, dependent on the amount of Na_2SO_4 and K_2SO_4 present in the ash [18].

The accelerated corrosion which is observed during biomass co-firing is as a result of exposure to the flue gas, containing harmful salts, known as alkali halides which

are produced during combustion. These alkali halides travel in the flue gas until they reach the superheater tube walls, where the temperatures are in the range of melting temperatures of the salts. The salts form a eutectic melt on the walls leading to further accumulation of the salts. Previous work has shown that the most severe corrosion problems in biomass fired boilers are associated with deposits containing these chlorides as opposed to the flue gas itself [19], [20]. The corrosion process follows a chemical process known as active oxidation, which is identified in Figure 1 and chemical reactions R1 to R5.



In this mechanism, alkali halide salts, typically in the form of alkali chlorides (MCl, where M represents K or Na), are released during the combustion process, travel in the flue gas and deposit on the tube walls and form a eutectic melt. Chlorine is released from the melt via a chemical reaction with the outer oxide (St_2O_3 , where St is Fe or Cr) layer of the metal (R1). One of the products of this reaction is free chlorine (Cl_2), which migrates to the oxide/metal interface and reacts with the uncorroded metal surface to form metal chloride initially as a solid (R2). This chloride then evaporates due to the high volatility of the chloride (R3).

The metal chloride diffuses outward to the oxide surface, where it reaches higher levels of oxygen concentration. Once oxygen partial pressure is increased sufficiently iron chloride is oxidized (R4). As the conversion of the metal chlorides to oxides (R4) occurs, cracks and pores grow in the oxide scale, leading to subsequent cracking and spalling, which results in a non-protective, loosely adherent oxide scale being formed [21]. The released chlorine is also now free to restart the cycle or is itself converted to HCl in the high moisture flue gas [22] (R5).

It has also been identified that the alkali sulfates present in the deposits may react with SO_2 and the metal oxides to form liquid alkali-metal sulfates according to reaction R6 [19], [23]. Additionally it has been shown that when alkalis come in contact with the protective chromium oxide layer, the alkalis react with the Cr_2O_3 to form alkali chromates, as shown in reaction R7. This chromate formation acts as a sink for the chromium, resulting in a loss of the oxide's protective properties. Subsequently the chlorine released as a product of R7 is free to react with the metal resulting in rapidly growing oxide scale, consisting of an outer hematite layer with an inner FeCr spinel-type oxide [24]–[27].

This paper will present a preliminary investigation of the effect of corrosion damage for P91 on creep rupture life for tubes at high temperature. Experiments have been carried out in order to determine a corrosion rate for tube wall loss in operational plants co-firing peat and biomass. SEM images and EDX element maps are presented and help to provide insight into the corrosion process and material degradation. An FE

methodology for a superheater tube undergoing creep and corrosion damage is presented.

The next section of this paper will describe the experimental methodology and the basis behind it. The modelling section will discuss the methods used for model validation, and for creep and creep-corrosion simulations. Results obtained from the experiments and the modelling are then discussed and compared, leading to the conclusions.

2. METHODOLOGY

2.1. Experimental

Tests have been carried out in order to obtain a realistic corrosion rate for the superheater tube wall loss. The experimental methodology used in the current work is similar to that used in work by Skrifvars et al., [28], [29] and has been described in more detail in [30], [31]. Synthetic salts were produced to represent ash compositions obtained from in-situ tests carried out by industrial collaborators for various levels of co-firing, for a 70% peat, 30% woodchip mixture. The chemical makeup of both the synthetic salt and in-situ ash are shown in Table 1 by weight percentage.

These synthetic salts were then applied to specimens of P91 steel obtained from industrial collaborators and placed in a furnace at 540 °C. Samples were removed from the furnace following 1, 4, 7, 14, 21 & 28 days exposure and fixed in epoxy. The samples were then cut to reveal a cross sectional area, ground using 240, 400, 800 and 1200 grit SiC grinding paper and polished progressively using 30, 6 and 3 µm diamond paste.

Samples were then examined using an Olympus BX51M optical microscope and a Hitachi S-4700 scanning electron microscope (SEM), to measure the depth of corrosion

and provide insight into the subsurface material degradation and structure of the corrosion layer. Energy dispersive X-ray spectroscopy (EDX) analysis was also carried out and element maps were created to obtain the complete chemical composition of a section of the sample. The experimental procedure has been discussed in more detail in previous work [30].

2.2. Computational

The present work presents a simplified model of the accelerated corrosion rates, which are present when co-firing biomass in power plants, combined with creep effects using the FE program Abaqus [32]. Initially creep effects were modelled on uniaxial test specimens. A simple superheater tube under closed-end conditions was then modelled. Initially the tube model was simulated with no damage effects; creep damage was then incorporated into the tube model, with corrosion effects being incorporated as a final step.

2.2.1. Creep Model

Creep damage was modelled based on the Kachanov, single variable creep damage equations [33], [34], given as Equations 1 to 5 and implemented via the user defined subroutine CREEP in Abaqus. Equations 1 to 3 are the multi-axial form of the creep damage equations.

$$\frac{d\varepsilon_{ij}^c}{dt} = \frac{3}{2} A' \left(\frac{\sigma_{eq}}{1 - \omega_C} \right)^n \frac{S_{ij}}{\sigma_{eq}} t^m \quad (1)$$

$$\frac{d\omega_C}{dt} = B' \frac{\sigma_r^\chi}{(1 - \omega_C)^\phi} t^m \quad (2)$$

$$\sigma_r = \alpha \sigma_1 + (1 - \alpha) \sigma_{eq} \quad (3)$$

where ε^c is creep strain, t is time, ω_C is the creep damage variable, σ_{eq} is equivalent stress, σ_r is rupture stress, σ_1 is maximum principal stress, S_{ij} is the deviatoric stress and A' , m , n , B' , χ , ϕ and α are material constants. Failure is assumed to occur when the damage term reaches a value of 1. Material constants for these equations have been obtained from the work carried out by Hyde et al.[10] at 650°C and are shown in Table 2.

2.2.2. Finite Element Model

A plain tube model is developed in Abaqus making use of the axial symmetric geometry. A schematic of the geometry and loading applied can be seen in Figure 2. The analysis was carried out for an elastic-creep material model, where a uniform wall temperature is assumed. Future models can include plasticity effects and temperature gradients through the wall.

Three different cases of internal pressures 10, 15 and 20 MPa were investigated, as this range captures typical operating pressures of in-situ tubes. The models were initially run with no creep damage or corrosion effects and results of hoop, axial and radial stress compared with Lamé's equations, which are shown as equations 4 to 6.

$$\begin{bmatrix} \sigma_H \\ \sigma_A \\ \sigma_R \end{bmatrix} = \left(\frac{p}{\left(\frac{R_o}{R_i}\right)^2 - 1} \right) \begin{bmatrix} \left(1 + \left(\frac{R_o}{r}\right)^2\right) \\ 1 \\ \left(1 - \left(\frac{R_o}{r}\right)^2\right) \end{bmatrix} \quad (4)$$

(5)

(6)

where p is the internal pipe pressure, R_o is the outer radius of the pipe, R_i is the inner radius of the pipe, r is the radius at any point through the wall thickness, σ_H is the hoop stress, σ_A is the axial stress and σ_R is the radial stress. Creep damage was then added to the model to investigate creep life without corrosion effects. Finally corrosion effects were added to the model.

2.2.3. Corrosion Model

Measurements of the oxide layer thickness are obtained from the experimental data. This oxide layer thickness is then related to the amount of substrate which was consumed in order to form the oxide scales, to determine the rate at which the substrate is corroded. This is done in a manner similar to that shown in previous work [30]. The main oxides produced in this form of corrosion are Fe_2O_3 , Cr_2O_3 and a mixed FeCr spinel-type oxide. For the purposes of this calculation, attention is focused on the iron in the alloy and the associated oxides. This is done as (1) P91 consists predominantly (90%) of iron and (2) the relevant physical properties (i.e. molecular weights and densities, which are required for the model) of the different oxides are similar in value.

Given that for every 2 moles of Fe removed from the substrate, 1 mole of Fe_2O_3 , for example, is deposited in the oxide layer as per reactions R2 and R4, the amount of moles of Fe are related to the number of moles of oxide formed via equation 7 .

$$\frac{dN_{Fe}}{dt} = 2 \frac{dN_{Fe_2O_3}}{dt} \quad (7)$$

where N_{Fe} is the number of moles of iron consumed and $N_{Fe_2O_3}$ is the number of moles of oxide produced. This is then related to the mass of the iron consumed and oxide produced via molecular weights as follows:

$$\frac{1}{M_{Fe}} \frac{dm_{Fe}}{dt} = \frac{2}{M_{Fe_2O_3}} \frac{m_{Fe_2O_3}}{dt} \quad (8)$$

where m_{Fe} is the mass of the iron consumed, $m_{Fe_2O_3}$ is the mass of oxide produced and $M_{Fe_2O_3}$ is the molecular weight of Fe_2O_3 . Hence, the rate of change of depth of substrate lost (l_{Loss}) is related to the rate of change of the oxide layer thickness (l_{Ox}) is produced as follows:

$$\frac{dl_{Loss}}{dt} = 2 \frac{M_{Fe}}{M_{Fe_2O_3}} \frac{\rho_{Fe_2O_3}}{\rho_{Fe}} \frac{dl_{Ox}}{dt} \quad (9)$$

Finally, an equation for l_{Loss} is obtained as follows:

$$l_{Loss} = 2 \frac{M_{Fe}}{M_{Fe_2O_3}} \frac{\rho_{Fe_2O_3}}{\rho_{Fe}} l_{Ox} \quad (10)$$

The experimental values for I_{Loss} are then obtained from the measured I_{Ox} values, as a function of time. A parabolic corrosion model, given by $I_{Loss} = a\sqrt{t}$ is hence used to describe the corrosion rate, where the constant a is identified using a least squares optimization technique:

$$a = \exp \left(\frac{\sum_{i=1}^n \ln I_{Loss,i} - 0.5 \sum_{i=1}^n \ln t_i}{n} \right) \quad (11)$$

where n is the number of experimental points used in the least squares calculation and t is time.

Corrosion is simulated here based on Arbitrary Lagrangian Eulerian (ALE) adaptive meshing capability available in Abaqus/Standard and defined using the user subroutine UMESHMOTION. This capability allows the boundaries of the FE mesh to be moved between analysis increments [32]. This technique has previously been used in die wear prediction [35], fretting wear prediction [36], and in the corrosion modelling of stents [37]. In this method material removal is simulated by the movement of nodes at the exterior of the mesh, simulating the incremental removal of material. As this method does not rely on element removal, it is less sensitive to mesh resolution. Additionally as the velocity of the node movement is determined via a user subroutine it can be defined to depend on, for example, species concentrations and fluxes on the corrosion surface as well as material stresses and strains in the vicinity of the surface [37].

Outer nodes of the oxide layer are defined as the nodes to be moved by UMESHMOTION as shown in Figure 3. All elements in the tube and oxide are defined as the adaptive mesh domain, allowing for a high-quality mesh to be maintained through the analysis. The adaptive meshing technique proceeds via two steps. Initially, the surface nodes are moved in the local normal direction, to simulate material removal, as a purely Eulerian analysis. Secondly, the material quantities are re-mapped to the new positions via advection by solving the advection equations using the second order Lax-Wendroff method [32], [36].

This subroutine is then combined with the creep and tube models resulting in a model showing a tube wall, undergoing uniform corrosion with creep damage effects. A flowchart detailing the main processes within the finite element creep-corrosion methodology is shown Figure 4. In the present work, continuum, axisymmetric 4 node elements are used to model the pipe wall.

3. RESULTS

3.1. Experimental

This section presents results obtained from experiments carried out on P91 samples exposed to synthetic salt at 540 °C for 1, 4, 7, 14, 21 and 28 days. SEM images and EDX element maps are presented and analysed. From these images, valuable insight into the mechanism of the corrosion process and the complex, time dependent structure of the corrosion layers is obtained.

Figure 5 shows SEM images of the specimen cross section area. Following 1 day exposure, poorly-adhered multilayers of oxides are visible, with voids formed above the substrate (Figure 5 (a)). These poorly-adhered multilayers of oxides form due to repeated cracking and spalling of the oxides [38], [39]. Examination of the sample exposed for 4 days (Figure 5 (b)) shows that the mixed oxide layer has travelled away from the substrate surface and now offers little protection against further corrosion. A second protective layer of oxide has formed close to the substrate surface and will slow the corrosion process.

The sample exposed for 7 days shows that the multi-layered oxide is again present far from the oxide layer. A second layer has also detached from the substrate and there is no evidence of the protective oxide layer (Figure 5 (c)). It is postulated that the protective oxide layer has detached from the substrate; this delamination effect can occur due to stresses in the oxide scales [40]. Following 14 days exposure (Figure 5 (d)) there is no evidence of a protective layer at the substrate surface but a number of layers which have detached from the substrate and moved away are visible. Similarly the sample exposed for 21 days (Figure 5 (e)), shows no evidence of protective oxide on the substrate surface; however, layers of oxide are visibly detached from the substrate. Figure 5 (f) shows the sample exposed for 28 days; from this numerous scales of multi-layers of oxide which have detached from the substrate surface can be seen.

EDX elemental maps of the cross sectional areas have been obtained showing the chemical compositions of sections of the samples. Maps are presented for the sample which was exposed for 4 days. Figure 6 shows the area of the 4 day sample

analysed and the corresponding element maps of Ca, S, O, Fe and Cr. Calcium and sulphur are clearly visible in the salt layer, as expected, (Table 1).

From these maps a mixed Cr/Fe, multi-layered oxide, which has detached from the substrate surface, is visible. Additionally a layer of iron oxide exists close to the substrate surface with a thin layer of chromium oxide tightly bound to the substrate between the iron oxide layer and the substrate. The presence of oxygen in the scales confirm they are oxides, while the absence of oxygen from the substrate confirms that it is uncorroded.

The oxide scales were measured for each sample removed from the furnace and a plot showing the evolution of the oxide layer thickness, (l_{ox}), with time is shown in Figure 7. It is difficult to obtain accurate measurements for samples exposed for long durations due to oxide fragmentation and spallation. The corrosion evolution follows a similar trend to that reported in similar work [41]. The initial breakdown of the protective oxide results in a large oxide layer thickness following 1 day of exposure.

Following this the corrosion proceeds at a more uniform rate. The initial breakdown can be, at least partially, attributed to the formation of alkali chromates, depleting the protective oxide layer of chromium, as shown in reaction R7. The oxide layer thickness obtained during this testing indicates far greater levels of corrosion than those obtained with no exposure to harmful salts. Fournier et al. [16] report a maximum thickness of 2.80 μm is reported following 36 days testing at 823 K with no salt exposure; here a maximum thickness of 31.77 μm is obtained following 28 days testing at 813 K with exposure to the synthetic salt.

3.2. Computational

Initial computational work focuses on model validation of the individual user subroutines and tube model. The creep model was compared successfully with test data obtained from work by Hyde et al. [10] and the results are shown in Figure 8.

Values obtained for I_{Ox} were then converted to I_{Loss} via equation 10 and the results are shown in Table 3. These results are then used to obtain the constant a from equation 11. Figure 9 shows the depth of substrate, I_{Loss} which has been removed in order to form the oxide layers. These measurements are then compared with results of the adaptive meshing technique and MATLAB results from equation 11 where the constant a has been identified as 3.349, where t is in days and I_{Loss} is in μm . The results are shown to agree satisfactorily.

In addition to the parabolic equation a bilinear fit was also considered for the model, as can be seen in Figure 9. While this initially appears to provide a more accurate prediction for I_{Loss} , following longer term exposure the bilinear fit would result in higher prediction for substrate consumed as can be seen in Figure 10. Therefore, in order to maintain a conservative approach to corrosion predictions the parabolic equation was used. The physical basis of the parabolic rate is that corrosion is controlled by diffusion of gas-phase reactants through the corrosion product layer [41], which is the mechanism here. In future an initial linear corrosion rate, followed by a parabolic rate may be considered.

Initial FE analyses are carried out with no damage effects and results are compared to theoretical values obtained from Lamé's equations 4 to 6. The creep and

corrosion effects are then added to the model and the effects on tube stresses and creep rupture life are investigated. The greatest change is with the hoop stress, which is initially highest at the tube interior but, following long-term creep and stress redistribution, becomes lowest at the interior of the tube.

Figure 11 (a) shows the evolution of hoop stress distribution in a pipe with an internal pressure of 15 MPa with increasing time. Initial elastic to steady-state stress redistribution is predicted to lead to reduced stress on the inside surface and increased stresses on the outside surface, e.g. for the case labelled 1,000 hours in Figure 11 (a). This stress redistribution occurs due to the time dependent creep deformation as described by Kraus [42] and has serious ramifications for the evaluation of the maximum stress in the tube.

Figure 11 (b) shows the hoop stress redistribution in a pipe with an internal pressure of 10 MPa with increasing time. The stress redistribution, resulting in the maximum hoop stress changing from the inner to outer tube wall is again evident. In addition to this increases in hoop stresses are found to occur with increases in time. This is attributed to the loss of healthy material from the tube wall due to corrosion. Corrosion of the tubes is hence shown to lead to a reduction of the load bearing capacity of the tubes resulting in early failure times.

The loss of wall thickness (l_{Loss}) is visible from Figure 11 (b). It is noted that the parabolic equation has calibrated a value for α based on experimental data up to a maximum time period of 672 hours, while the model runs in to the millions of hours for the 10 MPa case. However, previous work has shown that exposure of 7 days in a

furnace is sufficient to give reproducible and relevant information of the corrosion tendency of steels [29], additionally, the more conservative parabolic rate has been chosen for modelling the evolution of I_{Loss} .

Figure 12 shows contour plots of the hoop stress at increasing time periods, for the tube subjected to 20 MPa internal pressure. The loss of tube wall material due to corrosion is again evident from these plots. Additionally, the stress redistribution due to creep and the increase in hoop stress due to loss of wall thickness can be visually identified.

Figure 13 shows the predicted damage evolution for the three load cases (internal pressure of 10, 15 & 20 MPa), up to failure. For the three cases the effect of corrosion on life expectancy is visible. As expected, the longer the tubes are exposed, the greater the effect of corrosion, due to corrosion layer growth. The predicted life expectancy for the tubes subject to both creep and creep-corrosion damage is shown in Table 4 for the three load cases.

4. DISCUSSION

The current experiments do not include the impact flue gas has on the deposit, however, previous work has shown that testing in air produces corrosion products similar to those in corrosive environments [29]. Future work shall carry out tests in representative gaseous atmospheres. The extent of the internal attack, such as grain boundary degradation has not been included in the oxide layer measurements, or investigated in the current study. This is an important area of ongoing investigation with

the present research group, as microstructural degradation can result in a significant loss of strength in a material and reduce the life expectancy of a tube.

It is noted that the predicted time to failure of the 10 MPa case is of the order of millions of hours. In reality other damage mechanisms, such as fatigue, steamside corrosion, erosion and over-heating can be expected to cause failure before this time. In addition to these additional damage mechanisms, superheater tubes typically operate at higher pressures than 10 MPa. It is included here to capture the typical range of operating superheater tubes. Due to the extremely long life expectancy of the 10 MPa case there is a large effect of corrosion on the predicted life expectancy (44 %).

When compared with failures of superheater tubes from previous work [43], [44] the results are found to be of similar time frames. At an operating pressure of 17.65 MPa and temperature of between 430-460°C a superheater tube of T-12 steel ruptured following service time of 48,000 hours, while a creep analysis based on material hardness and the Larson-Miller parameter predicted a rupture time of 562,941 hours for an operating pressure of 14.1 MPa at 499°C [43]. Additionally tubes of Sa-210 Grade A-1 steel had previously been reported to have a predicted creep rupture time of 42,267 hours at a pressure of 17.45 MPa with the tubes rupturing following 33,270 hours of operation. A 12Cr1MoV steel at 600°C and 17.45 MPa was given a predicted creep rupture life of approximately 45,000 hours [44]. These times correspond well with the predicted life expectancies of the tubes shown in Table 4.

It should also be noted that the modelled corrosion rate did not include microstructural damage. Future studies will investigate how the corrosion process

affects the material microstructure. Future work will also develop a 3D model of pipe bends, where stress concentrations are expected to give earlier failure. The creep data used here corresponded to accelerated creep tests at 650°C. At lower temperatures, such as those associated with the corrosion tests (540°C) reported here, the creep rupture life would significantly increase, leading to significantly increased corrosion effects, as demonstrated by the 10 MPa case shown in Table 4, for example. Similarly, it can be expected that the rate of corrosion will increase with increasing temperature. Future work will focus on a broader range of temperatures for corrosion, creep and creep-corrosion testing and characterization.

5. CONCLUSIONS

The corrosion mechanism which occurs when P91 steel is exposed to synthetic salt, representative of ash obtained during biomass co-firing at high temperatures was studied. SEM images and EDX element maps have provided a key insight into the corrosion process. Scales, consisting of multi-layered oxides are shown to form and detach from the substrate via repeated cracking and spalling of the oxides. These oxides lose both their protective properties against further corrosion, and load bearing capability due to the repeated cracking and subsequent detachment from the substrate. This results in an extremely high corrosion rate when compared to samples tested without exposure to salts.

An FE methodology is presented for pipes under internal pressure. The effect of corrosion and creep damage on the stresses through the wall thickness and on the life expectancy of a tube is shown. Results have been compared between tubes subjected solely to creep damage and to creep-corrosion damage. The model shows that the

longer the exposure time to the corrosive environment, the greater the effect on rupture life expectancy.

ACKNOWLEDGMENTS

This work is co-funded by the Irish Research Council, ESB and Bord na Móna under the Enterprise Partnership Scheme (EPSPG/2012/466). The authors would like to acknowledge contributions from Dr. Fionn Griffin from ESB and Mr. Barry Hooper from Bord na Móna, industrial collaborators in this project. The authors acknowledge the facilities and technical assistance of the NCBES Electron Microscopy unit within the Centre for Microscopy & Imaging at NUI Galway, a facility funded by NUI Galway and the Irish Government's programme for Research in Third Level Institutions, Cycles 4 and 5, National Development Plan 2007-2013. The authors also acknowledge contributions made by collaborators of the METCAM project, which is supported by Science Foundation Ireland under Grant Number SFI/10/IN.1/I3015.

REFERENCES

- [1] M. Hupa, "Ash-Related Issues in Fluidized-Bed Combustion of Biomasses: Recent Research Highlights," *Energy & Fuels*, vol. 26, no. 1, pp. 4–14, Jan. 2012.
- [2] F. Jappe Frandsen, "Utilizing biomass and waste for power production—a decade of contributing to the understanding, interpretation and analysis of deposits and corrosion products," *Fuel*, vol. 84, no. 10, pp. 1277–1294, Jul. 2005.
- [3] A. U. Syed, N. J. Simms, and J. E. Oakey, "Fireside corrosion of superheaters: Effects of air and oxy-firing of coal and biomass," *Fuel*, vol. 101, pp. 62–73, Nov. 2012.
- [4] J. S. Dubey, H. Chilukuru, J. K. Chakravartty, M. Schwienheer, A. Scholz, and W. Blum, "Effects of cyclic deformation on subgrain evolution and creep in 9-12% Cr-steels," *Mater. Sci. Eng. A*, vol. 406, pp. 152–159, 2005.
- [5] F. Abe, "Precipitate design for creep strengthening of 9% Cr tempered martensitic steel for ultra-supercritical power plants," *Sci. Technol. Adv. Mater.*, vol. 9, p. 013002, 2008.
- [6] R. A. Barrett, T. P. Farragher, C. J. Hyde, N. P. O'Dowd, P. E. O'Donoghue, and S. B. Leen, "A Unified Viscoplastic Model for High Temperature Low Cycle Fatigue of Service-Aged P91 Steel," *J. Press. Vessel Technol.*, vol. 136, no. 2, p. 021402, 2014.
- [7] K. Zarrabi, "Estimation of boiler tube life in presence of corrosion and erosion processes," *Int. J. Press. Vessel. Pip.*, vol. 53, pp. 351–358, 1993.
- [8] J. Purbolaksono, a. Khinani, a. Z. Rashid, a. a. Ali, and N. F. Nordin, "Prediction of oxide scale growth in superheater and reheater tubes," *Corros. Sci.*, vol. 51, no. 5, pp. 1022–1029, May 2009.
- [9] R. Viswanathan, S. R. Paterson, H. Grunloh, and S. Gehl, "Life Assessment of Superheater/Reheater Tubes in Fossil Boilers," *J. Press. Vessel Technol.*, vol. 116, no. 1, pp. 1–16, Feb. 1994.
- [10] T. H. Hyde, A. A. Becker, W. Sun, and J. A. Williams, "Finite-element creep damage analyses of P91 pipes," *Int. J. Press. Vessel. Pip.*, vol. 83, no. 11–12, pp. 853–863, Nov. 2006.
- [11] T. H. Hyde, A. A. Becker, W. Sun, A. Yaghi, A. Thomas, and P. Seliger, "Finite Element Creep Failure Analyses of P91 Large Tensile Cross-Weld Specimens

Tested At 625 O C,” in *5th International Conference on Mechanics and Materials in Design*, 2006, pp. 1–12.

- [12] M. R. Wenman, K. R. Trethewey, S. E. Jarman, and P. R. Chard-Tuckey, “A finite-element computational model of chloride-induced transgranular stress-corrosion cracking of austenitic stainless steel,” *Acta Mater.*, vol. 56, no. 16, pp. 4125–4136, Sep. 2008.
- [13] K. Sawada, M. Fujitsuka, M. Tabuchi, and K. Kimura, “Effect of oxidation on the creep rupture life of ASME T23 steel,” *Int. J. Press. Vessel. Pip.*, vol. 86, no. 10, pp. 693–698, 2009.
- [14] B. Fournier, M. Sauzay, C. Caës, M. Noblecourt, M. Mottot, A. Bougault, V. Rabeau, J. Man, O. Gillia, P. Lemoine, and A. Pineau, “Creep-fatigue oxidation interactions in a 9Cr-1Mo martensitic steel . Part II : Effect of compressive holding period on fatigue lifetime,” *Int. J. Fatigue*, vol. 30, pp. 663–676, 2008.
- [15] B. Fournier, M. Sauzay, C. Caës, M. Noblecourt, M. Mottot, a. Bougault, V. Rabeau, J. Man, O. Gillia, P. Lemoine, and a. Pineau, “Creep-fatigue-oxidation interactions in a 9Cr-1Mo martensitic steel. Part III: Lifetime prediction,” *Int. J. Fatigue*, vol. 30, pp. 1797–1812, 2008.
- [16] B. Fournier, M. Sauzay, C. Caës, M. Noblecourt, M. Mottot, a. Bougault, V. Rabeau, and a. Pineau, “Creep-fatigue-oxidation interactions in a 9Cr-1Mo martensitic steel. Part I: Effect of tensile holding period on fatigue lifetime,” *Int. J. Fatigue*, vol. 30, pp. 649–662, 2008.
- [17] R. W. Swindeman, M. L. Santella, P. J. Maziasz, B. W. Roberts, and K. Coleman, “Issues in replacing Cr-Mo steels and stainless steels with 9Cr-1Mo-V steel,” *Int. J. Press. Vessel. Pip.*, vol. 81, pp. 507–512, 2004.
- [18] F. Masuyama, “History of power plants and progress in heat resistant steels,” *ISIJ Int.*, vol. 41, no. 6, pp. 612–625, 2001.
- [19] H. P. Nielsen, F. J. Frandsen, K. Dam-Johansen, and L. L. Baxter, “The implications of chlorine-associated corrosion on the operation of biomass-fired boilers,” *Prog. Energy Combust. Sci.*, vol. 26, pp. 283–298, 2000.
- [20] D. A. Tillman, D. Duong, and B. Miller, “Chlorine in Solid Fuels Fired in Pulverized Fuel Boilers s Sources , Forms , Reactions , and Consequences : a Literature Review †,” *Energy & Fuels*, vol. 23, pp. 3379–3391, 2009.

- [21] H. Asteman and M. Spiegel, "Investigation of the HCl (g) attack on pre-oxidized pure Fe, Cr, Ni and commercial 304 steel at 400°C," *Corros. Sci.*, vol. 49, no. 9, pp. 3626–3637, Sep. 2007.
- [22] H. J. Grabke, E. Reese, and M. Spiegel, "The effects of chlorides, hydrogen chloride and sulfur dioxide in the oxidation of steels below deposits," *Corros. Sci.*, vol. 37, no. 7, pp. 1023–1043, 1995.
- [23] D. O. Albina and N. J. Themelis, "Theory and experience on corrosion of waterwall and superheater tubes of waste-to-energy facilities," Department of Earth and Environmental Engineering Fu Foundation School Of Engineering and Applied Science Columbia University, 2005.
- [24] J. Pettersson, J.-E. Svensson, and L.-G. Johansson, "KCl-Induced Corrosion of a 304-type Austenitic Stainless Steel in O₂ and in O₂ + H₂O Environment: The Influence of Temperature," *Oxid. Met.*, vol. 72, no. 3–4, pp. 159–177, Apr. 2009.
- [25] J. Pettersson, N. Folkesson, L. G. Johansson, and J. E. Svensson, "The effects of KCl, K₂SO₄ and K₂CO₃ on the high temperature corrosion of a 304-type austenitic stainless steel," *Oxid. Met.*, vol. 76, pp. 93–109, 2011.
- [26] S. Karlsson, J. Pettersson, L.-G. Johansson, and J.-E. Svensson, "Alkali Induced High Temperature Corrosion of Stainless Steel: The Influence of NaCl, KCl and CaCl₂," *Oxid. Met.*, vol. 78, pp. 83–102, 2012.
- [27] J. Lehmusto, B.-J. Skrifvars, P. Yrjas, and M. Hupa, "Comparison of potassium chloride and potassium carbonate with respect to their tendency to cause high temperature corrosion of stainless 304L steel," *Fuel Process. Technol.*, vol. 105, pp. 98–105, Jan. 2013.
- [28] B.-J. Skrifvars, R. Backman, M. Hupa, K. Salmenoja, and E. Vakkilainen, "Corrosion of superheater steel materials under alkali salt deposits Part 1: The effect of salt deposit composition and temperature," *Corros. Sci.*, vol. 50, no. 5, pp. 1274–1282, May 2008.
- [29] B.-J. Skrifvars, R. Backman, M. Hupa, K. Salmenoja, and M. Westén-Karlsson, "Corrosion of super-heater steel materials under alkali salt deposits. Part 2: SEM analyses of different steel materials," *Corros. Sci.*, vol. 52, no. 3, pp. 1011–1019, Mar. 2010.
- [30] C. P. O'Hagan, B. J. O'Brien, F. Griffin, B. Hooper, S. B. Leen, and R. F. D. Monaghan, "Porosity-Based Corrosion Model for Alkali Halide Ash Deposits during Biomass Co-firing," *Energy & Fuels*, vol. 29, no. 5, pp. 3082–3095, 2015.

- [31] C. P. O'Hagan, B. J. O'Brien, S. B. Leen, and R. F. D. Monaghan, "Experimental Characterisation of Materials for Biomass Co-Firing," in *Proceedings of the 22nd European Biomass Conference and Exhibition*, 2014, no. 22, pp. 23–26.
- [32] Anon., "Abaqus analysis manual v6.12." DS SIMULIA, Rhode Island, USA, 2012.
- [33] I. Kachanov, LM, "Akad Naul," *Akad. Nauk. SSSR*, vol. 8, no. 26, 1958.
- [34] D. R. Hayhurst, "Creep rupture under multi-axial states of stress," *J. Mech. Phys. Solids*, vol. 20, no. 6, pp. 381–382, Dec. 1972.
- [35] C. Wang, J. Chen, Z. C. Xia, and F. Ren, "Die wear prediction by defining three-stage coefficient K for AHSS sheet metal forming process," *Int. J. Adv. Manuf. Technol.*, vol. 69, pp. 797–803, 2013.
- [36] T. Zhang, P. E. McHugh, and S. B. Leen, "Computational study on the effect of contact geometry on fretting behaviour," *Wear*, vol. 271, no. 9–10, pp. 1462–1480, 2011.
- [37] J. A. Grogan, S. B. Leen, and P. E. McHugh, "Optimizing the design of a bioabsorbable metal stent using computer simulation methods," *Biomaterials*, vol. 34, no. 33, pp. 8049–60, Dec. 2013.
- [38] A. Zahs, M. Spiegel, and H. J. Grabke, "Chloridation and oxidation of iron, chromium, nickel and their alloys in chloridizing and oxidizing atmospheres at 400–700°C," *Corros. Sci.*, vol. 42, no. 6, pp. 1093–1122, 2000.
- [39] H. J. Grabke, M. Spiegel, and A. Zahs, "Role of Alloying Elements and Carbides in the Chlorine-Induced Corrosion of Steels and Alloys," *Mater. Res.*, vol. 7, no. 1, pp. 89–95, 2004.
- [40] T. Hussain, a. U. Syed, and N. J. Simms, "Trends in fireside corrosion damage to superheaters in air and oxy-firing of coal/biomass," *Fuel*, vol. 113, pp. 787–797, 2013.
- [41] H. P. Nielsen, F. J. Frandsen, and K. Dam-Johansen, "Lab-Scale Investigations of High-Temperature Corrosion Phenomena in Straw-Fired Boilers," *Energy & Fuels*, vol. 13, pp. 1114–1121, 1999.
- [42] H. Kraus, *Creep analysis*. John Wiley & Sons Canada, Limited, 1980.
- [43] J. Ahmad, M. M. Rahman, M. H. a Zuhairi, S. Ramesh, M. a. Hassan, and J. Purbolaksono, "High operating steam pressure and localized overheating of a

primary superheater tube," *Eng. Fail. Anal.*, vol. 26, no. February 2011, pp. 344–348, 2012.

- [44] H. Shokouhmand, B. Ghadimi, and R. Espanani, "Failure analysis and retrofitting of superheater tubes in utility boiler," *Eng. Fail. Anal.*, vol. 50, pp. 20–28, 2015.

Figure Captions List

Figure 1	Image showing the active oxidation process; images of tubes in-situ and tubes following removal from plant [30]
Figure 2	Dimensions and mechanical loading of P91 pipe
Figure 3	FE model showing direction of nodal movement
Figure 4	Flowchart detailing the user subroutines implemented in Abaqus
Figure 5	SEM images of P91 after exposure to synthetic salt at 540°C for (a) 1 day; (b) 4 days; (c) 7 days; (d) 14 days; (e) 21 days; (f) 28 days
Figure 6	SEM image and EDX element maps of sample exposed to synthetic salt for 4 days
Figure 7	Thickness of oxide layer following exposure to synthetic salt
Figure 8	Creep curves obtained from F.E analysis compared with experimental data from Hyde et al. [10]
Figure 9	Depth of substrate removed following exposure compared with model and bilinear fit
Figure 10	Comparison of bilinear rate vs parabolic rate for long term corrosion
Figure 11	Hoop stress redistribution and increase with time at (a) 15 MPa and (b) 10 MPa
Figure 12	Abaqus plots for 20 MPa internal pressure showing hoop stress distribution and growing oxide layer with time
Figure 13	Damage curve for superheater tube with internal pressure of (a) 10 MPa, (b) 15 MPa, (c) 20 MPa

Figures

Figure 1

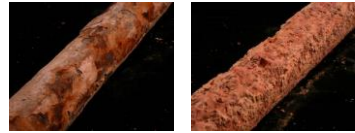
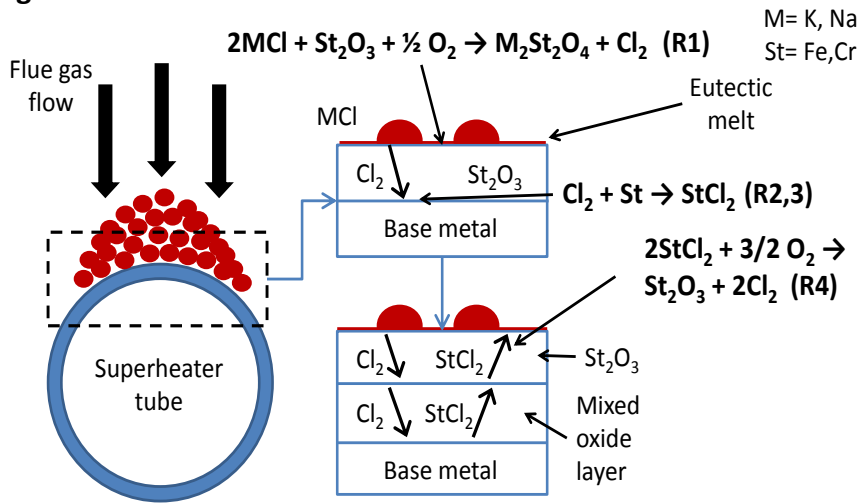


Figure 2

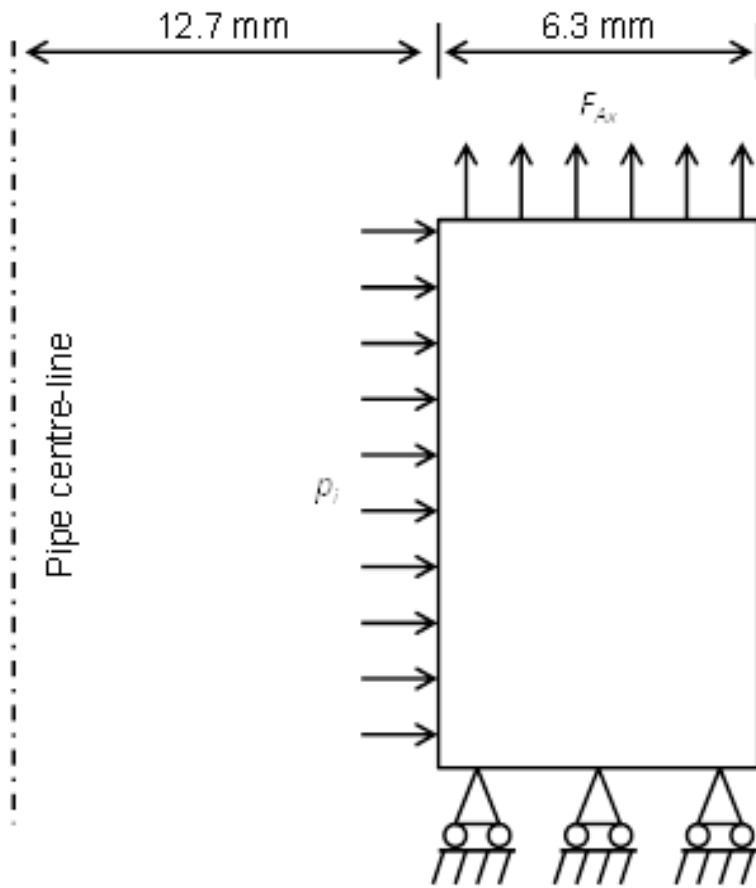


Figure 3

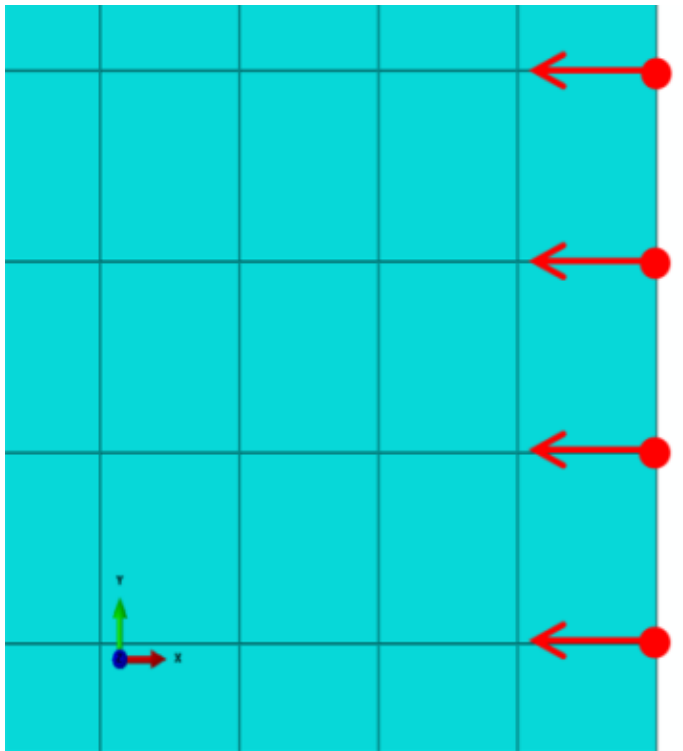


Figure 4

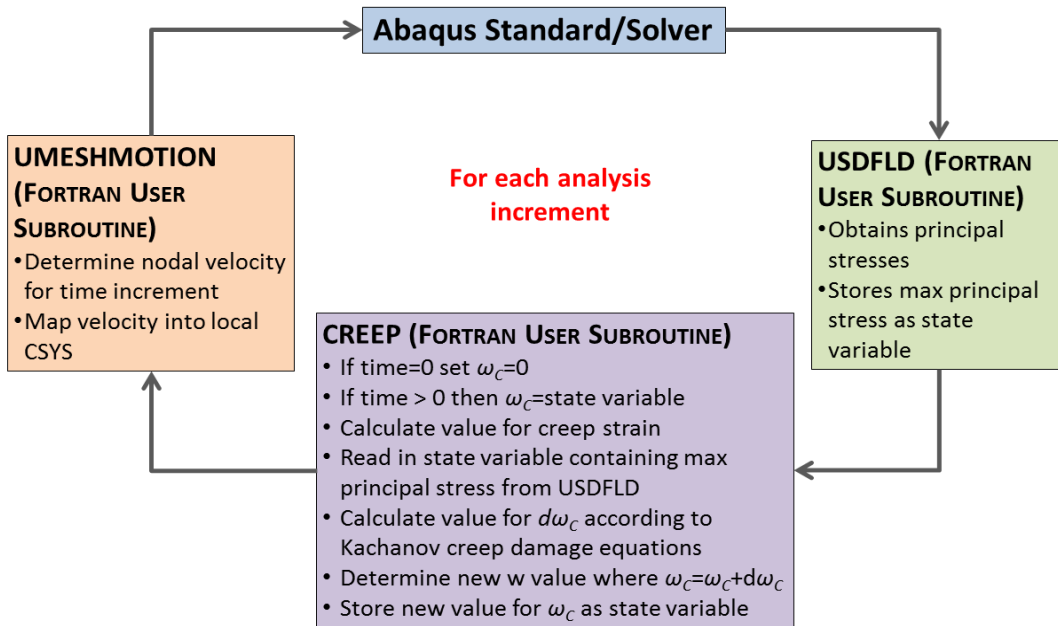


Figure 5

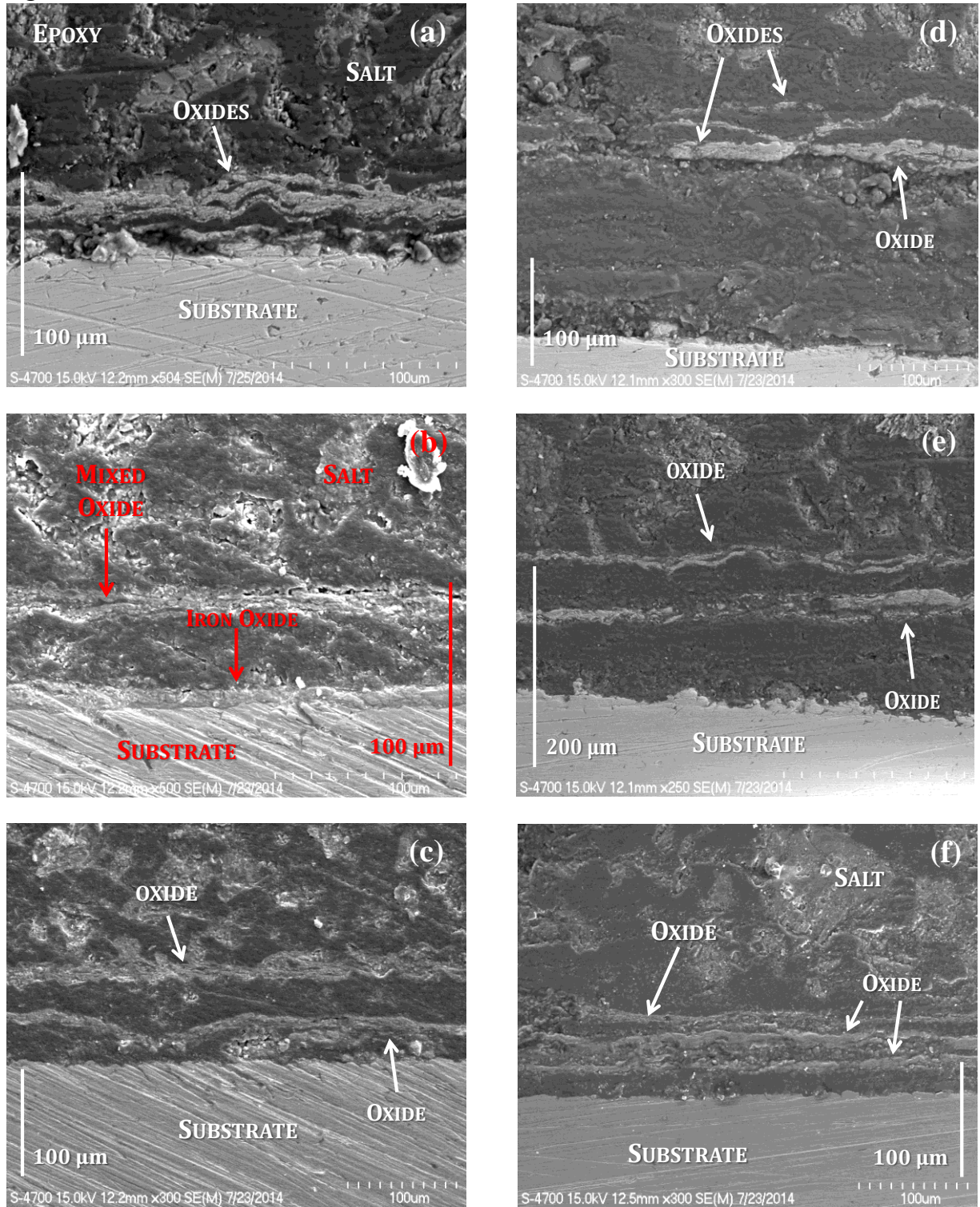


Figure 6

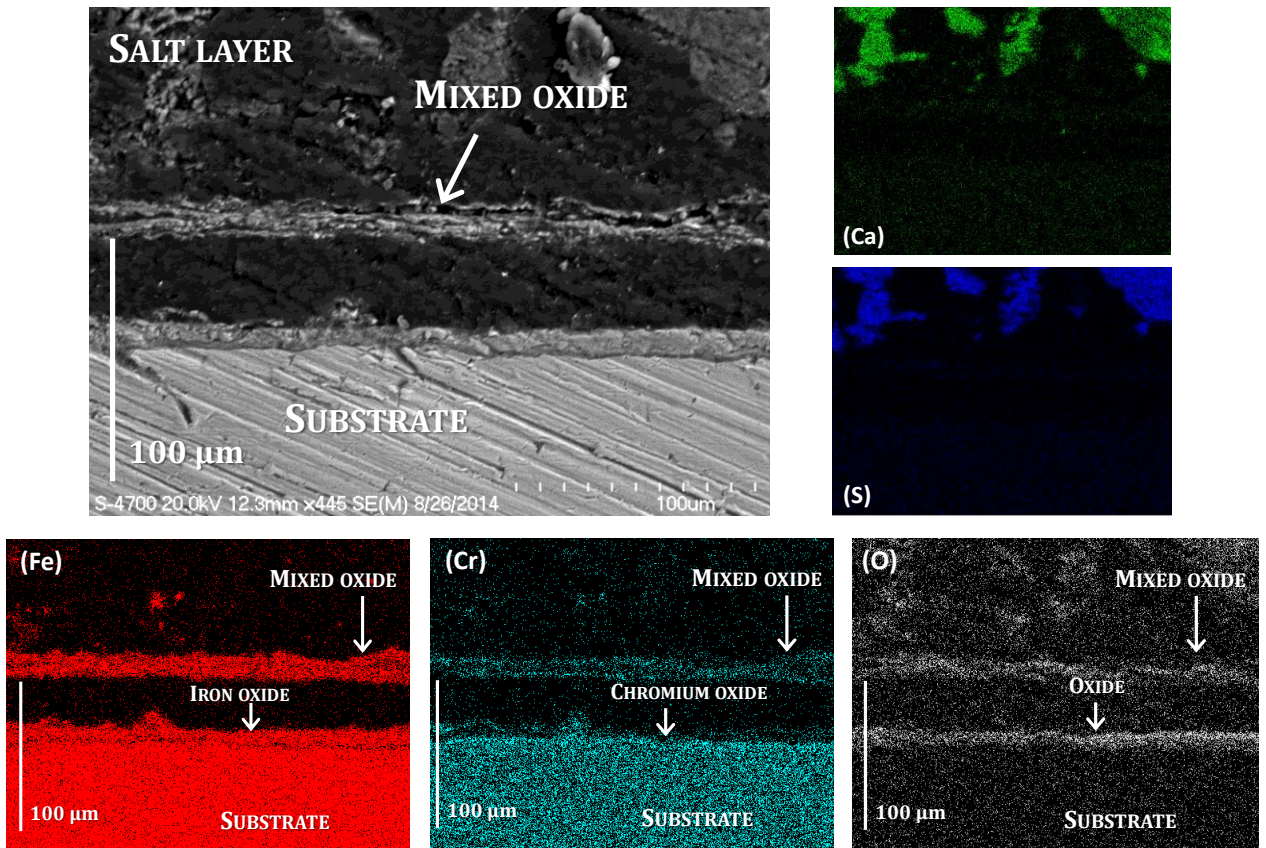


Figure 7

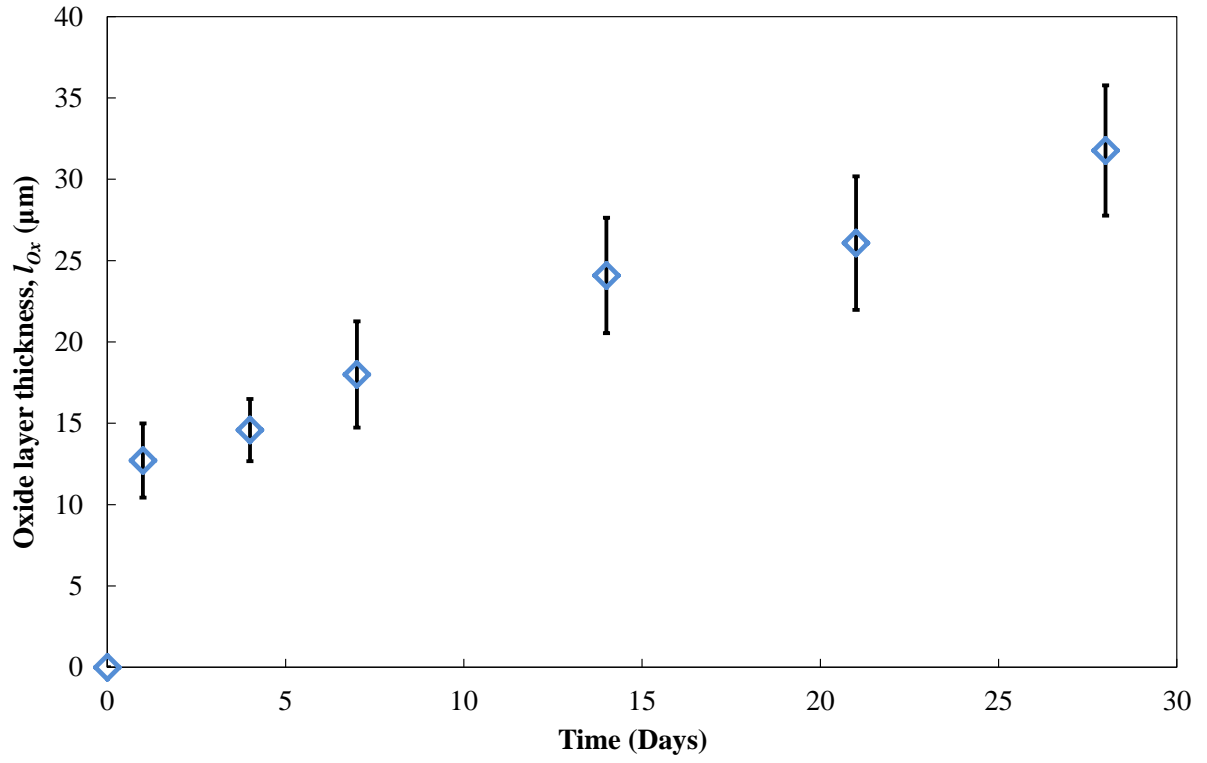


Figure 8

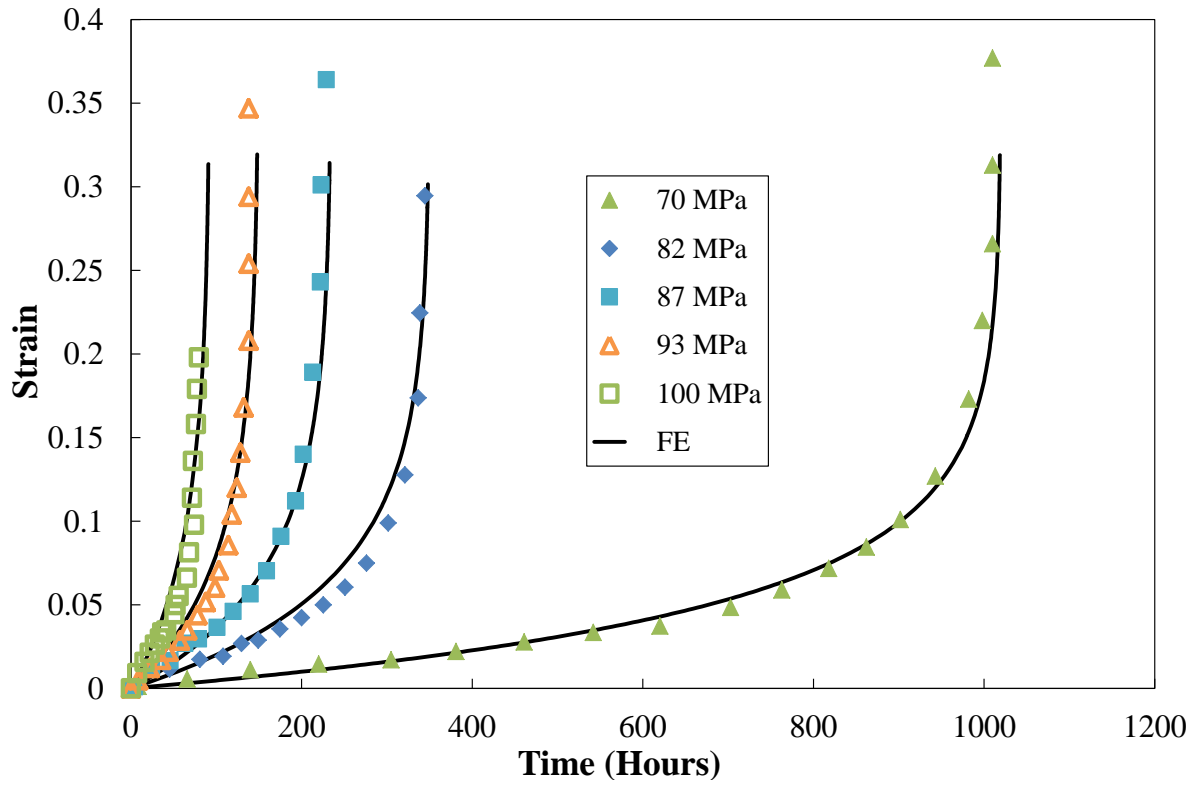


Figure 9

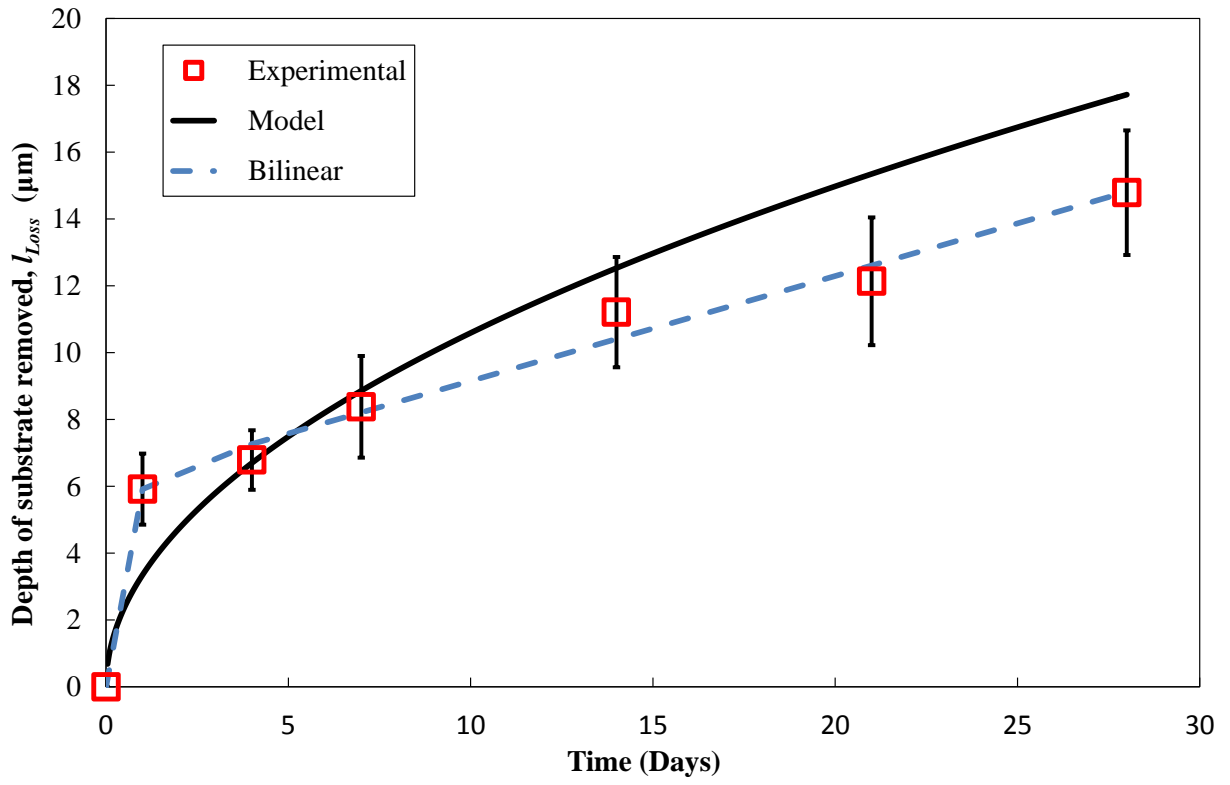


Figure 10

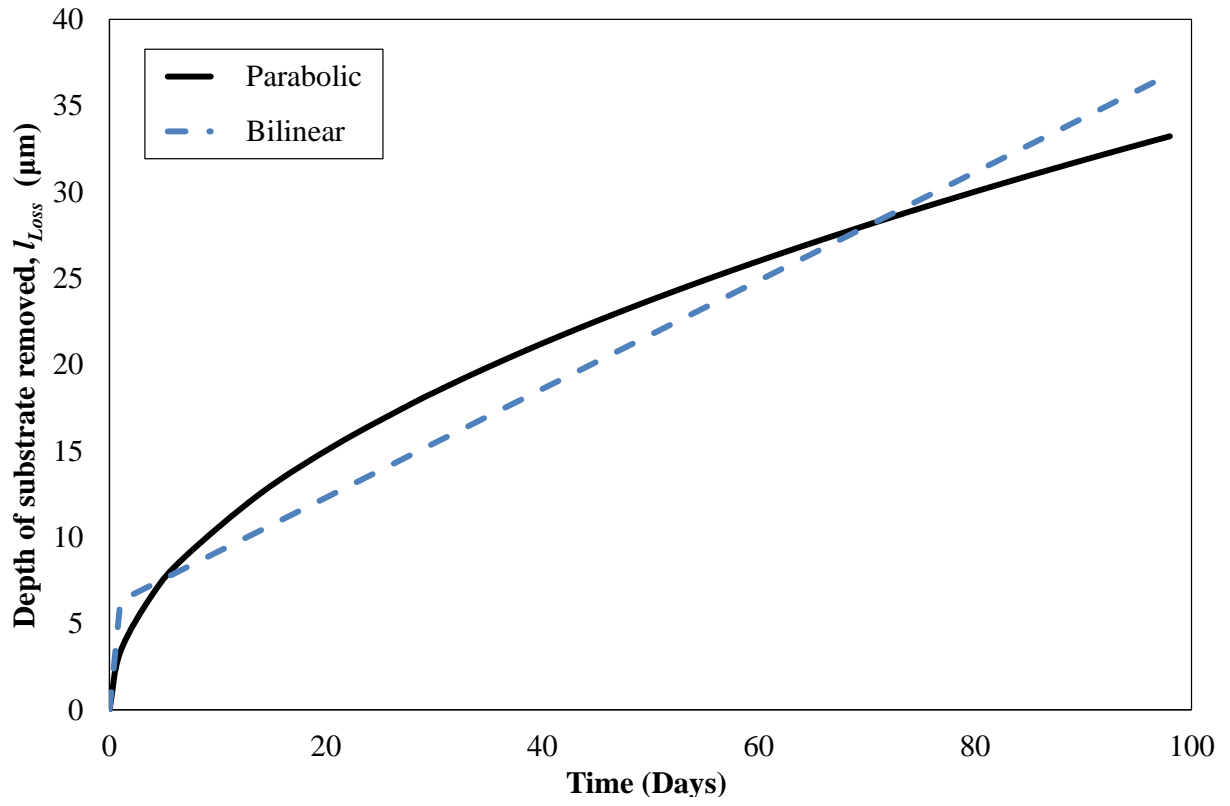


Figure 11

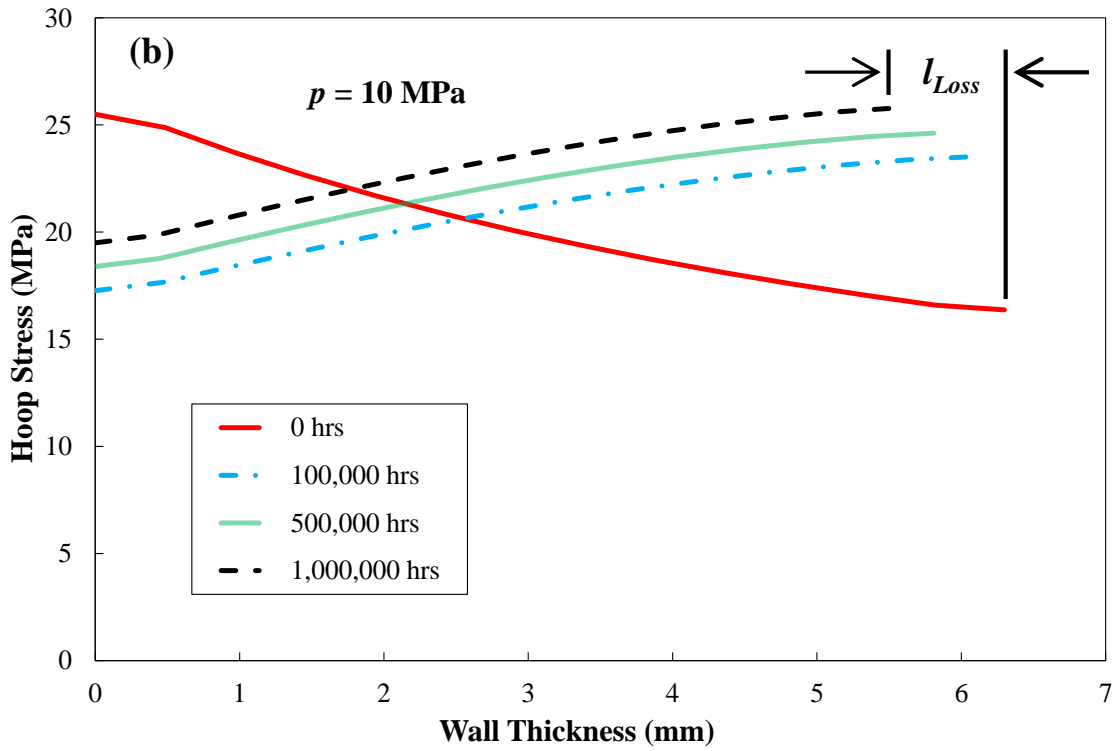
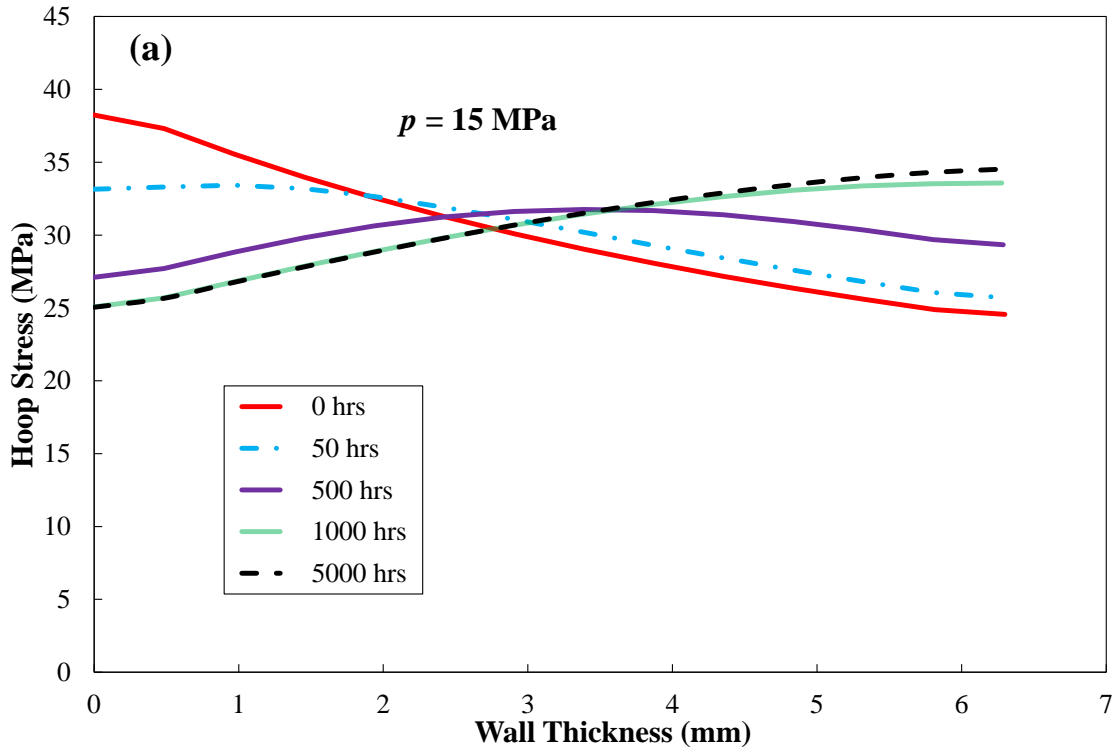


Figure 12

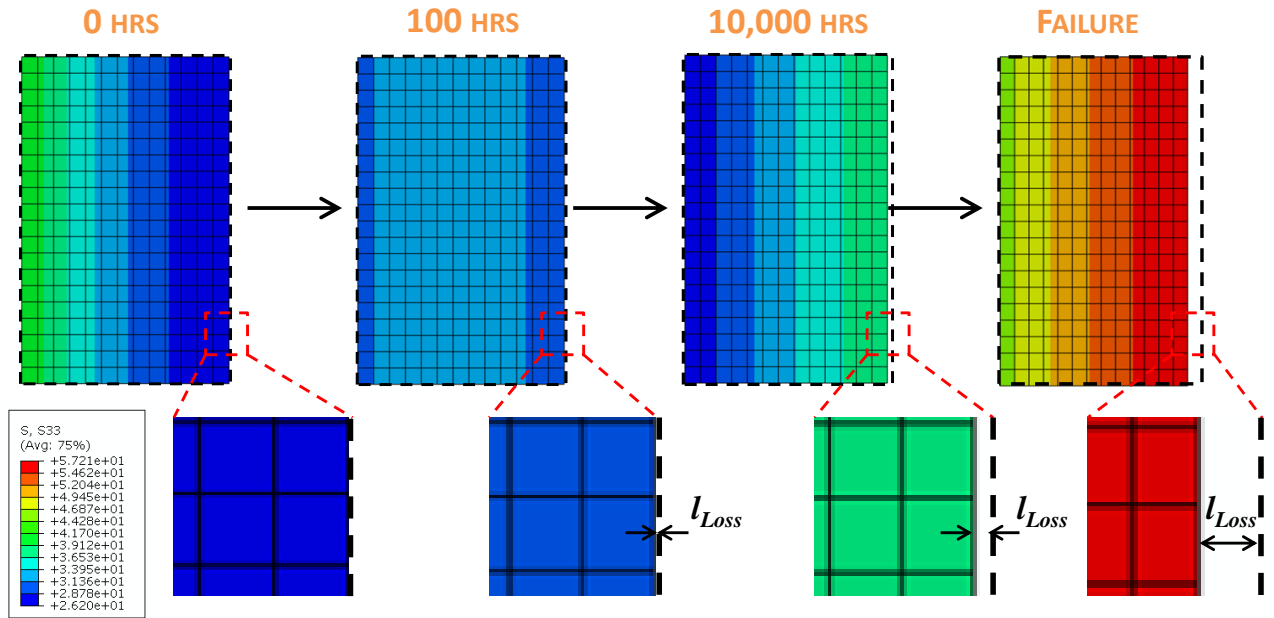
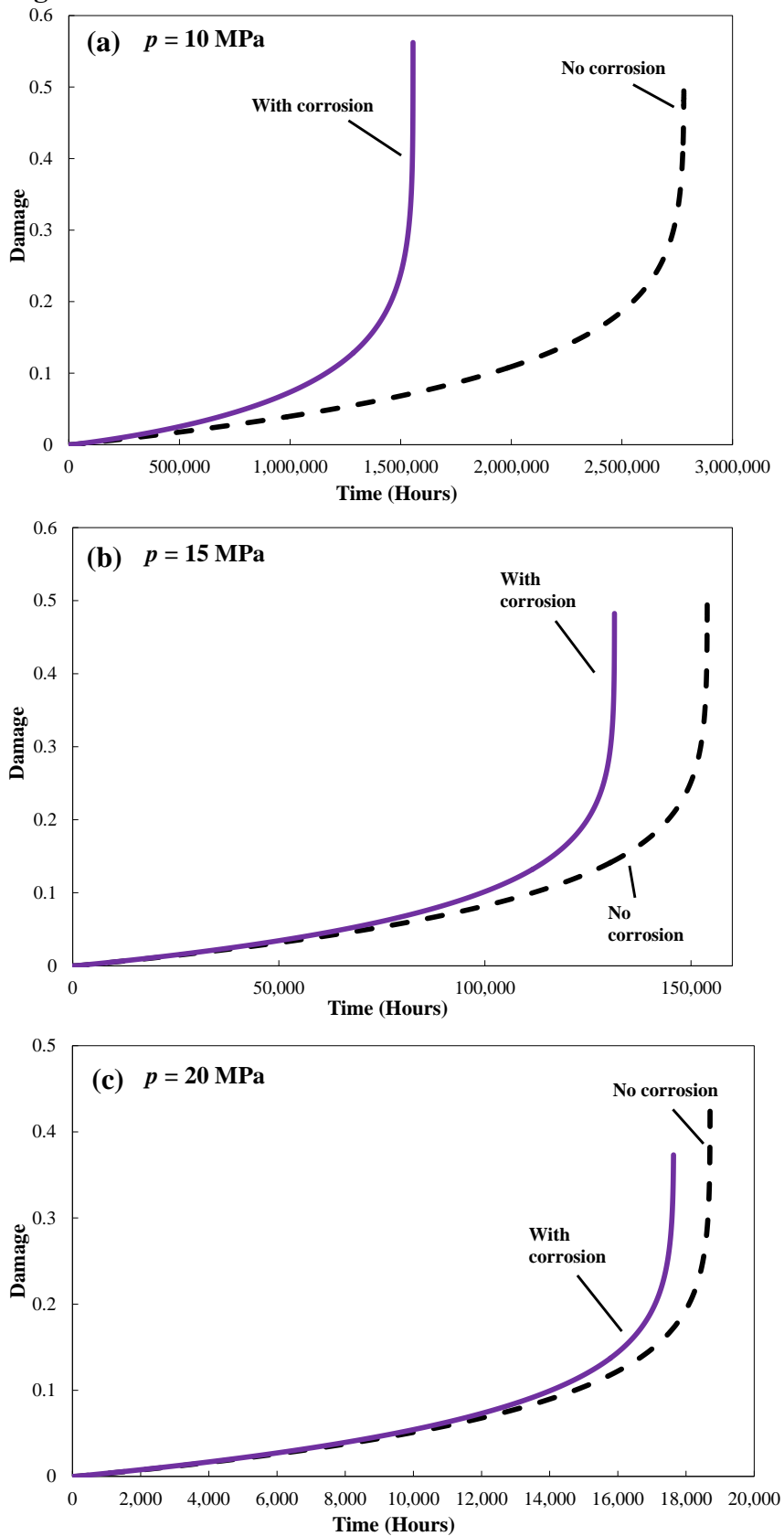


Figure 13



Tables

Table Caption List

Table 1	Compositions of ash deposition from a 70:30 peat woodchip mixture and representative synthetic salt
Table 2	Material constants used in creep equations (obtained from Hyde et al. [10] for P91 at 650°C)
Table 3	Values for oxide layer thickness, l_{O_x} , and depth of substrate consumed, l_{Loss}
Table 4	Time to failure for creep and creep corrosion cases

Table 1

<i>Element wt. %</i>	<i>Na</i>	<i>K</i>	<i>Cl</i>	<i>Br</i>	<i>S</i>	<i>Mg</i>	<i>Ca</i>	<i>Si</i>	<i>Fe</i>	<i>Al</i>	<i>Ni</i>	<i>P</i>	<i>Cr</i>
Plant ash deposit	2.09	5.21	2.18	0.07	21.59	3.54	44.35	5.87	9.70	1.70	0.94	1.51	1.23
Synthetic salt	2.12	5.27	2.29	0.07	42.25	3.36	44.36	-	-	-	-	-	-

Table 2

<i>A'</i>	<i>n</i>	<i>m</i>	<i>B'</i>	ϕ	χ	α
1.092×10^{-20}	8.462	-4.754×10^{-4}	3.537×10^{-17}	7.346	6.789	0.215

Table 3

<i>Days</i>	<i>1</i>	<i>4</i>	<i>7</i>	<i>14</i>	<i>21</i>	<i>28</i>
<i>l_{Ox} (μm)</i>	12.7	14.6	18.0	24.1	26.1	31.8
<i>L_{Loss} (μm)</i>	5.9	6.8	8.4	11.2	12.1	14.8

Table 4

<i>Int. Pressure (MPa)</i>	<i>Creep (hrs)</i>	<i>Creep-Corrosion (hrs)</i>	<i>Decrease in life (%)</i>
<i>10</i>	2,779,970	1,555,670	44.0
<i>15</i>	153,933	131,429	14.6
<i>20</i>	18,704	17,632	5.7